Friction **12**(7): 1512–1531 (2024)
https://doi.org/10.1007/s40544-023-0830-y
ISSN 2223-7690
CN 10-1237/TH
RESEARCH ARTICLE

Effect of fatigue load on the bending tribo-corrosion-fatigue behaviors between the main cable wires

Bo WANG[1], Dagang WANG[1,*], Jihong YE[2], Liang TANG[1], Hailang CHONG[1], Wei XU[1], Xinxin ZHANG[1], Jianhao CHEN[3], Haiyan DENG[4], Jie ZHANG[5], Guowen YAO[6], Magd Abdel WAHAB[7]

[1] *School of Mechatronic Engineering, China University of Mining and Technology, Xuzhou 221116, China*

[2] *Xuzhou Key Laboratory for Fire Safety of Engineering Structures, China University of Mining and Technology, Xuzhou 221116, China*

[3] *National Wire Rope Quality Inspection Center, Nantong Product Quality Supervision and Inspection Institute, Nantong 226011, China*

[4] *Jiangsu Langshan Wire Rope Co., Ltd., Nantong 226003, China*

[5] *School of Mechatronic Engineering, Southwest Petroleum University, Chengdu 610500, China*

[6] *School of Civil Engineering, Chongqing Jiaotong University, Chongqing 400074, China*

[7] *Soete Laboratory, Faculty of Engineering and Architecture, Ghent University, Zwijnaarde B-9052, Belgium*

Received: 24 April 2023 / Revised: 11 July 2023 / Accepted: 20 September 2023

Abstract: The main cable bent around the saddle of the suspension bridge is subjected to the wind, the vehicle, the bridge's own weight and the corrosive media. The coupling of the three loads and the environments causes the friction, the corrosion, and the fatigue (tribo-corrosion-fatigue) among the wires inside the main cable. In this paper, a wire bending tribo-corrosion-fatigue test rig was designed and developed. The effect of fatigue load on the bending friction behaviors between the cable wires in ultrapure water and 3.5% NaCl solution was explored. The tribological properties and electrochemical corrosion behaviors under different fatigue loading ranges were investigated. The tribo-corrosion-fatigue interaction between the cable wires was quantitatively characterized, and the mechanism of the interaction was analyzed. The results demonstrate that the increasing fatigue load exacerbates the coupling damage of the cable wires attributed to the enhanced interaction. The findings carry theoretical importance when assessing the main cable's deterioration and the load-bearing safety of a suspension bridge.

Keywords: bending; tribo-corrosion-fatigue; interaction; parallel steel wires; fatigue load

1 Introduction

The characteristics of large span, strong load-bearing capacity, beautiful appearance, and convenient erection make the long-span multi-tower suspension bridges widely used [1]. The main cable bends around the saddle groove. It is the key load-bearing component of the bridge, and its failure will cause the instability of bridge structure or even collapse [1, 2]. In the service process, the suspension bridge is subjected to the coupling action of the dead load (stiffened beam, deck system, main cable, etc.), the wind load, the live load (automobile load, etc.) and the salt spray environment (NaCl, $MgCl_2$, etc.) [3–6]. These lead to the friction, corrosion, and fatigue behaviors between the parallel wires inside the main cable at the main saddle. This is the bending tribo-corrosion-fatigue behaviors of the cable wires. It reduces the effective cross-sectional area of the cable wires, decreasing the load-bearing capacity of the wires, and seriously affect the bearing safety of the main cable in the suspension bridge [1, 2]. Therefore, revealing the bending tribo-corrosion-fatigue behaviors of the cable wires is very important to improve the

* Corresponding author: Dagang WANG, E-mail: wangdg@cumt.edu.cn

load-bearing safety and reliability of main cable and ensure the service reliability of suspension bridge.

Many theories and experiments have been used to explored the tribo-fatigue properties of the steel wires or ropes [7–9]. Some wear evolution models and characteristics of steel wire under diverse operational circumstances are formulated and examined by employing finite element simulation and conducting tribological tests [10–13]. The corrosion research of the steel wire or wire rope is mainly to add corrosive solution environment on the basis of the above tribo-fatigue or friction wear test, or to employ pre-corroded wire or rope for testing [14, 15]. Within the realm of studying suspension bridge main cables or wires, a few scholars have conducted a small amount of research on the contact slip and damage behavior of the main cable by means of simulation and experiment. Using statics theory, Wang et al. [16] explored the mechanical properties of the main cable, investigating the impact of pretension, applied load and friction coefficient on stress distribution, contact conditions and slip behaviors of individual strands or wires along the arc contact paths within the saddle. These analyses were conducted through the application of the finite element method. The accuracy of the finite element models was confirmed through a practical test involving the assessment of friction and slip between the strands and the saddle. Furthermore, a custom-designed dynamic contact testing apparatus was utilized to investigate the dynamic contact and interactive behaviors between parallel wires and the materials of the saddle [4, 17]. The study presented the dynamic contact characteristics of the saddle material during friction cycles, highlighting the influence of transverse and longitudinal positions, friction cycles, and saddle materials on these dynamic contact behaviors. Karanci and Betti [5, 6] introduced a technique to assess the residual capacity of cables and put forward a methodology that utilizes environmental condition data to estimate the annual corrosion rate, taking into account various environmental factors. Liu et al. [18] designed a specialized test system to study the behaviors of bridge wires when subjected to the combined effects of corrosion, fretting, and fatigue. The findings indicate that the coupling scar resulting from this combination can surpass the cumulative depth of both the fretting fatigue scar and the corrosion pit individually. Guo et al. [19] conducted a comprehensive set of fretting fatigue experiments, varying the parameters of fretting and fatigue, to examine the tribological properties, fretting fatigue behavior, and fracture failure mechanism of bridge cables. Nonetheless, there has been limited exploration regarding the bending tribo-corrosion-fatigue interactions among parallel wires within the main cable, particularly when subjected to specific curvatures. Furthermore, there is a dearth of qualitative analysis and quantitative characterization pertaining to the interplay of friction, corrosion, and fatigue in such scenarios. Unlike the straightforward combination of electrochemical corrosion and mechanical tribo-fatigue, the distinctive characteristic of bending tribo-corrosion-fatigue damage lies in the intricate interplay, whether positive or negative, between bending tribo-fatigue and corrosion. This interaction defines the nature of the damage observed in such cases [20]. The progression of tribo-fatigue damage is facilitated by electrochemical corrosion, while in turn, the tribo-fatigue damage expedites the process of corrosion [21]. Consequently, the wear volume loss observed in wire tribo-corrosion-fatigue cannot be solely attributed to the sum of volume losses from pure electrochemical corrosion and pure bending tribo-fatigue. It encompasses an additional volume loss stemming from the intricate interaction between electrochemical corrosion and tribo-fatigue [20, 22, 23]. Therefore, accurately quantifying the tribo-corrosion-fatigue interaction holds immense importance in effectively assessing the damage incurred by the main cable in suspension bridges.

This study aims to comprehensively examine the impact of fatigue load on the bending tribo-corrosion-fatigue behaviors observed among parallel wires within the main cable of suspension bridges, both qualitatively and quantitatively. The structure of this paper is arranged as follows: following the introductory section, the subsequent section delves into the specifics of the bending tribo-corrosion-fatigue test. Section 3 of this paper provides a comprehensive examination of the influence of fatigue load on tribological and electrochemical corrosion behaviors across various mediums, along with a detailed quantitative analysis

of the tribo-corrosion-fatigue interaction. The conclusions drawn from this study are then presented in Section 4.

2 Experimental details

2.1 Materials and parameters

The 1.4 mm diameter high-strength wire, treated with hot-dip galvanization, is employed for the test. The contact length between the fatigue and contact wires is set at 60 mm. The contact wire and fatigue wire are hot-dip galvanized steel wires produced in the same batch. The wires used in this experiment belong to a commonly employed type of steel wire found in the main cables of suspension bridges. The test wire in this experiment is the fatigue wire. The wire material analyzed in this study primarily comprises 94.77% iron (Fe), 2.87% carbon (C), 0.57% manganese (Mn), 0.36% silicon (Si), 0.75% phosphorus (P), 0.45% sulfur (S), and 0.24% chromium (Cr). The wire exhibits various mechanical properties, including an elastic modulus of 166 GPa, the ultimate strength of 1,650 MPa, the nominal fracture true strain of 0.482, the yield strength of 1,601 MPa, the section shrinkage of 38.3% and the minimum cross-sectional area at neck reduction of 0.9503 mm^2 [2]. The fatigue wire forms a wrapping angle of 48° with the contact wires in this experimental setup [4, 17].

To investigate the impact of fatigue load on the tribo-corrosion-fatigue behaviors among parallel wires, three distinct fatigue load ranges of 750–1,000 N, 750–1,200 N, and 750–1,400 N are chosen for test [2]. The remaining experimental parameters include a relative displacement ranging from 300–500 μm, a frequency of 6 Hz, a winter room temperature of approximately 5 °C, and a total of 2×10^5 fatigue cycles. The corrosion solution used in this study is a specially prepared 3.5% NaCl solution, consisting of analytically pure NaCl particles dissolved in ultrapure water. The control group in this study is formed by conducting the tribo-fatigue test in ultrapure water without the presence of corrosion.

2.2 Test rig and methods

Figure 1 illustrates the wire tribo-corrosion-fatigue test rig employed in this study. To eliminate the surface oxide film as much as possible, 2,500 mesh sandpaper was used for gently polishing before the test. The ultrasonic cleaning of the wires with alcohol was used to remove the surface oil as much as possible. First, the contact wires were fixed to the

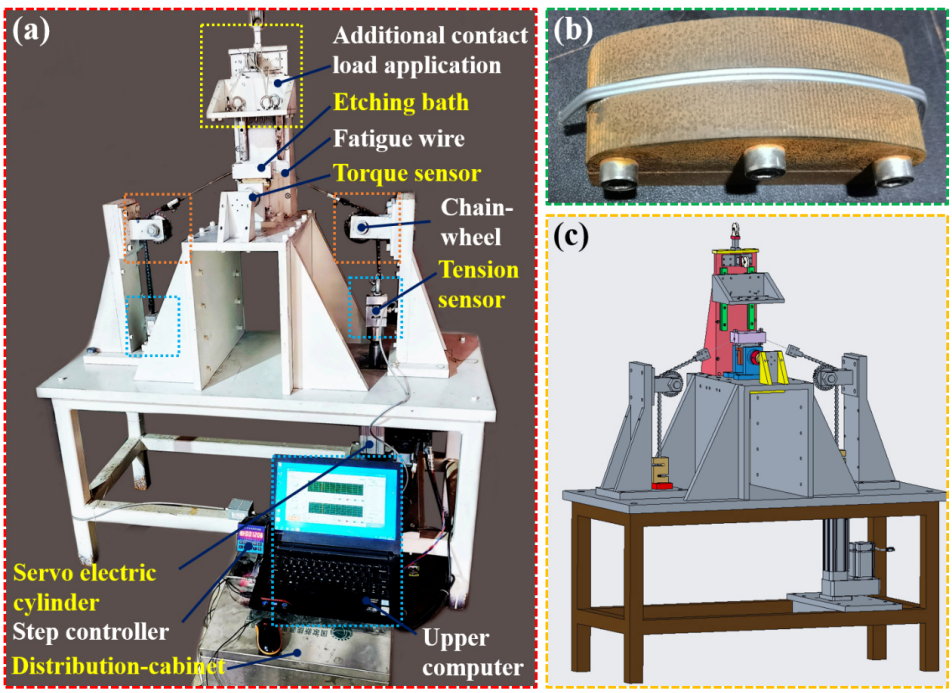

Fig. 1 Bending tribo-corrosion-fatigue test rig (a) photo show, (b) clamp with contact wires, and (c) three-dimensional diagram.

contact clamp (Fig. 1(b)), and then fixed to the corresponding position of the test rig. The fatigue wire, cleansed and measuring 490 mm in length, was securely fastened onto both the left and right clamps. Subsequently, the stepping controller was used to adjust the expansion distance of the electric cylinder, ensuring proper contact between the fatigue wire and the contact wires. Once the fatigue load reached approximately 200 N, the etching bath was installed, and the joint was sealed using a sealant, which was then air-dried at room temperature. Either the 3.5% NaCl corrosion solution or ultrapure water was introduced, causing the immersion of both the fatigue wire and the contact clamp in the solution. Ultimately, by configuring the appropriate program and utilizing the stepping controller, the servo motor was controlled to engage the electric cylinder, thereby pulling the fatigue wire. The upper computer acquisition software closely monitored the tension sensor until the desired maximum fatigue load was attained. The test commenced by initiating the servo electric cylinder, and the tension data was continuously recorded during the test. Following the completion of the test, the fatigue wire, along with the worn area, was carefully severed, followed by a thorough wash with alcohol to eliminate any remnants of the surface corrosion solution. The fatigue wire samples were subsequently air-dried at room temperature and securely placed into sample bags in preparation for further analysis.

Electrochemical tests were carried out immediately after the test by using the CHI604E electrochemical analyzer from Shanghai CH Instruments Co., Ltd. A saturated calomel electrode was chosen as the reference electrode (CE), while a platinum sheet electrode served as the auxiliary electrode (RE). The sample being tested was designated as the working electrode (WE). To achieve stabilization, the wire samples were submerged in an electrolyte solution (3.5% NaCl solution) for a duration of 30 minutes prior to the initiation of the test. Firstly, the initial step involved measuring the open-circuit potential, followed by conducting electrochemical impedance spectrum tests at the open-circuit potential. These tests were performed using an amplitude of 0.005 V and a scanning frequency range spanning from 100 kHz to 0.01 Hz. The obtained data from the electrochemical impedance spectrum test was subjected to fitting analysis using ZView 2 software (version 3.1, Solartron Metrology, UK). Then, the dynamic method was employed, involving a slow continuous scanning of the control electrode potential, accompanied by the measurement of the instantaneous current values corresponding to the respective potentials. The complete polarization curve can be obtained by plotting the instantaneous current against the corresponding electrode potential. The test was conducted within a potential range of −1.6–0.6 V, utilizing a scanning rate of 0.01 V/s. By applying the Tafel extrapolation method, the Tafel region of the polarization curve was extended until reaching the corrosion potential, allowing for the determination of the wire sample's corrosion current. The corrosion current density within the worn area of the fatigue wire can be determined by evaluating the ratio of the corrosion current to the test area. To assess the corrosion resistance of the fatigue wire across different wear degrees, the representative worn area of the 10 mm fatigue wire was selected due to the difficulty in testing the entire worn area, which was long in length.

For the qualitative characterization of the wire samples, the surface morphology and element distribution were examined using a scanning electron microscope (SEM, SU3500, Hitachi, Japan) with X-ray energy dispersive spectrometry (EDS, QUANTAX XFlash, Bruker, Germany). To obtain quantitative data, the size of the wear scar profile was measured utilizing a high-speed digital microscope system (VW-9000, Keyence) from Japan, allowing for comprehensive observation and analysis.

2.3 Data processing and calculation methods

According to the application of Euler's formula in physics (Eq. (1)), the friction coefficient between the parallel wires can be calculated by Eq. (2). By choosing a specific number of valid data points within each cycle, the average friction coefficient for that cycle can be calculated [24, 25]. The average friction coefficient of a certain number of periods according to the data volume interval was chosen to draw the friction coefficient curves.

$$F_1 = (F_2 - F_1)\mathrm{e}^{\mu\theta'} \tag{1}$$

$$\mu = \frac{1}{\theta'} \ln \frac{F_2}{F_1} \tag{2}$$

where, F_1 and F_2 represent the measured tension sensor values at the wire's two ends, N. θ' is the wrapping angle between the contact wires and the fatigue wire, rad. μ denotes the friction coefficient.

As shown in Fig. 2(a), the contact area undergoes a transition from line contact to surface contact, resulting in a long and narrow rectangular contact surface. To quantify this, the wear width was measured using a high-speed digital microscopic system. The fatigue wire was divided into 5 sections. On average, 3 measuring points were chosen for each section at random, and each measuring point was subjected to 5 repeated measurements. Two wear marks need to be measured. Finally, the wear width of the fatigue wire was determined by calculating the average value of 150 measured data points. Figure 2(b) shows the cross-section of the wear scar, where the missing circular area represents the cross-sectional failure area denoted as S. As shown in Fig. 2(c), AB is the wear width l, CD is the wear depth h, r represents the radius of the wire, θ represents the angle between OA and OC. The following formula can be deduced from the geometric relationships.

$$\theta = \arcsin \frac{l}{2r} \tag{3}$$

$$h = r - r\cos\theta \tag{4}$$

$$S = 2r^2\theta - 2r^2 \sin\theta\cos\theta \tag{5}$$

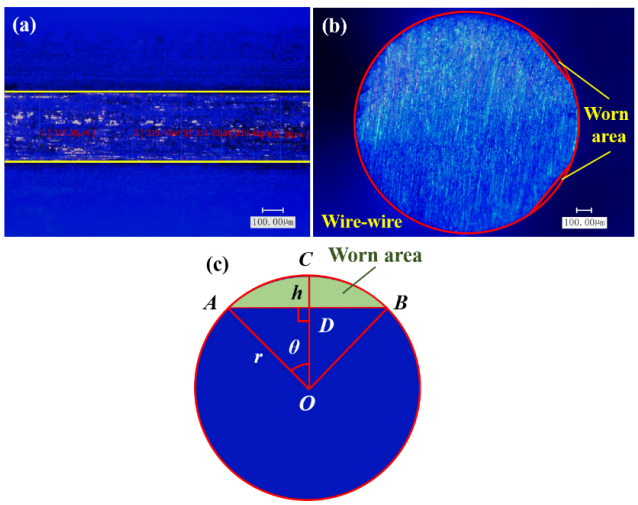

Fig. 2 Wear scar profile (a) top view, (b) cross-sectional view, and (c) geometric diagram

The total volume loss of fatigue wire (V) in 3.5% NaCl solution and the volume loss of pure wear (V_{wear}) in ultrapure water were determined by multiplying the cross-sectional failure area S with the wear length (60.5 mm). The average wear rate was defined as the amount of wear volume experienced per unit of time, expressed as the ratio between the wear volume and the duration of wear.

3 Results and discussion

3.1 Friction coefficient

As shown in Fig. 3(a), the friction coefficients of different fatigue load ranges present the same trend of rapid increase—gradual decrease—slow increase—stabilization. Due to the limitations of the experimental conditions, the steel wire could not be completely cleaned. In addition, the cleaned wire is not immediately used for the test, which leads to the reoxidation and pollution of the steel wire. Therefore, the sharp rise observed in the early stage can be attributed to the rapid elimination of the uncleared oxide film and oil film from the wire surface under stress, leading to a significant increase in the friction coefficient. Due to incomplete running-in of the wire contact surface and the presence of significant surface roughness, the friction coefficient is high. As the fatigue cycles increase, the bumps on the wire surface collide with each other during the relative sliding. The surface produces adhesive and plastic deformation, forming tiny wear, which gradually decreases the surface roughness. Therefore, the friction coefficient decreases gradually. The fatigue wire is repeatedly subjected to stress as the test proceeds. Microscopic deformation occurs on the wire surface. Adhesion and fatigue flaking form fine abrasive particles, which are continuously ploughed between contact surfaces under the drive of friction, resulting in three-body wear [26]. The wire surface roughness increases slightly. Under the tensile stress, once the generation and discharge of abrasive particles reach a dynamic equilibrium, the friction coefficient gradually stabilizes. Moreover, the larger the maximum fatigue load is, the sooner the friction coefficient reaches stabilization, as this can be attributed to the increased likelihood of contact between the smaller bumps and

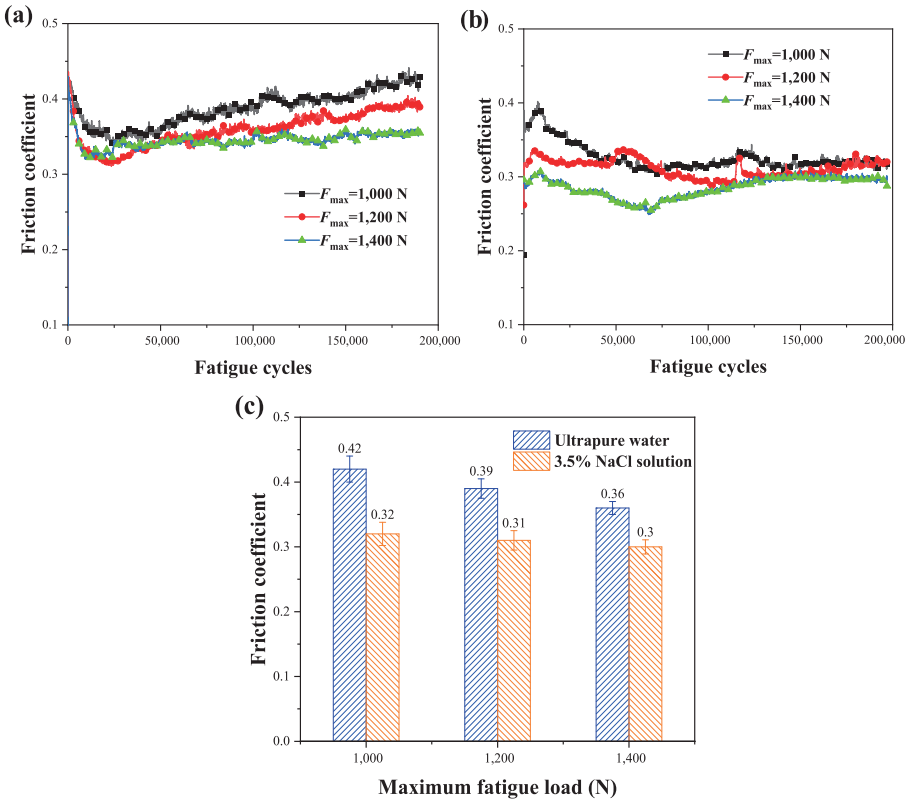

Fig. 3 Friction coefficient in (a) ultrapure water and (b) 3.5% NaCl solution. (c) Average value when subjected to different fatigue loads.

pits on the contact surfaces, resulting in deformation. The more intense the wear, the shorter the time it takes to reach the stable wear, and the easier the friction coefficient is to stabilize. Once reaching a relatively stable state, the average friction coefficients for different maximum fatigue load of 1,000 N, 1,200 N and 1,400 N are recorded as 0.42, 0.39 and 0.36, respectively (Fig. 3(c)). The friction coefficient decreases as the fatigue load increases. This phenomenon can be attributed to the curved contact of the wire, which leads to an increase in pressure on the contact surface with the progressive increment of the fatigue load. While the increase in wear width and wear morphology indicates an expansion in the actual contact area (Figs. 4 and 6, shown in Sections 3.2 and 3.3), the rise in pressure does not exhibit a proportional relationship with the actual contact area. In fact, the increase in pressure surpasses the expansion of the actual contact area, resulting in a decrease in the friction coefficient [12, 27]. The friction coefficient demonstrates a similar variation trend under various fatigue loads in 3.5% NaCl solution and bears resemblance to its behavior in ultrapure water (Fig. 3(b)). At the initial stage, the friction coefficient also presents a rapid increase trend, the reason is the same as that in ultrapure water. However, the corrosive media induces the passivation of the wire surface, so the friction coefficient decreases later than that in ultrapure water. The wire surface roughness gradually decreases with the increasing fatigue cycles, gradually decreasing the friction coefficient. The corrosive medium makes the passivation film continuously formed and destroyed, and the zinc coating is constantly consumed (as shown in Fig. S1 and Table S1, provided in the Electronic Supplementary Material (ESM)), so the friction coefficient decreases for a long time. When the zinc coating wears out, the wear mainly occurs between the wire substrate. The Cl^- in 3.5% NaCl solution accumulates at the defects on the substrate surface, constantly eroding the wire, making the removal of surface material easy, and two-body wear becomes three-body wear. The third body in this experiment includes the steel wire substrate material, the passivated film material on the wire surface and the corrosion product (produced in 3.5% NaCl solution). The third body participates in the wear process and

finally loses in the form of wear debris and ions [28, 29]. The wear between the wire substrate intensifies, the wear area increases constantly, increasing the actual contact area. As a result, the friction coefficient gradually increases. In ultrapure water, the minimum time for friction coefficient to stabilize is observed at the maximum fatigue load of 1,400 N. Once reaching a table state, the average friction coefficients for maximum fatigue load of 1,000, 1,200 and 1,400 N are measured at 0.32, 0.31 and 0.30, respectively.

An interesting observation is that the friction coefficient in ultrapure water exceeds that in a 3.5% NaCl solution. This can be attributed to the persistent plowing of hard debris between the contact surfaces along the sliding direction in ultrapure water, induced by tensile stress, resulting in an increase in surface roughness (Fig. 5). In the corrosive environment, Cl^- ions possess distinctive characteristics such as a small ionic radius, high penetration ability, and strong affinity for adsorption onto metal surfaces [30], which accelerates local corrosion. The corrosion-induced spalling on the surface of the steel wire is notable, and the predominant third body consists of a loose, lamellar structure that can be easily removed. Additionally, the surface roughness is lower compared to that observed in ultrapure water, resulting in a smaller friction coefficient. In addition, the presence of corrosion in 3.5% NaCl solution leads to an increasing surface defects on the steel wire. The third body formed by the exfoliation of material and the adhesion to the surface exhibits a loose and flexible structure. Under the action of compressive stress, it is rapidly compressed and converted into a third body layer with a certain bearing capacity [31, 32], which decreases the friction coefficient. This contributes to the earlier attainment of the stable stage for the friction coefficient in 3.5% NaCl solution compared to that in ultrapure water (Fig. 3(b) vs. Fig. 3(a)). However, without the influence of corrosion, the third body is mainly granular and has a relatively strong hardness in ultrapure water. The third body particles are cut on the contact surface, producing a large number of ploughings (Fig. 5). The third body layer is difficult to form, which causes the friction coefficient to climb continuously and the stabilization to be delayed (Fig. 3(a) vs. Fig. 3(b)). The fluctuation of the friction coefficient occurs due to the generation and overflow of the wear debris, as well as the disruption and reformation of the third body layer, involving the transformation between two-body contact and three-body contact.

3.2 Wear mechanisms

In particular, the wear morphologies in 3.5% NaCl solution at different cycles at the maximum fatigue load of 1,400 N are discussed (Fig. 4). At the fatigue

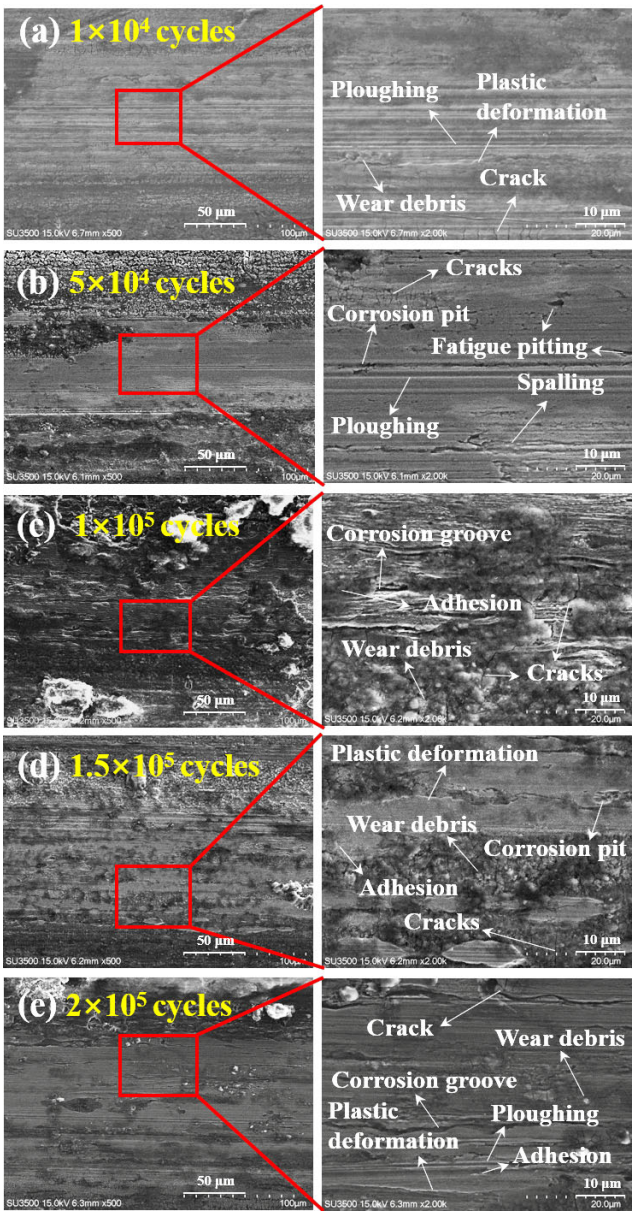

Fig. 4 Wear morphologies of fatigue wires when subjected to different fatigue cycles at the maximum fatigue load of 1,400 N in 3.5% NaCl solution

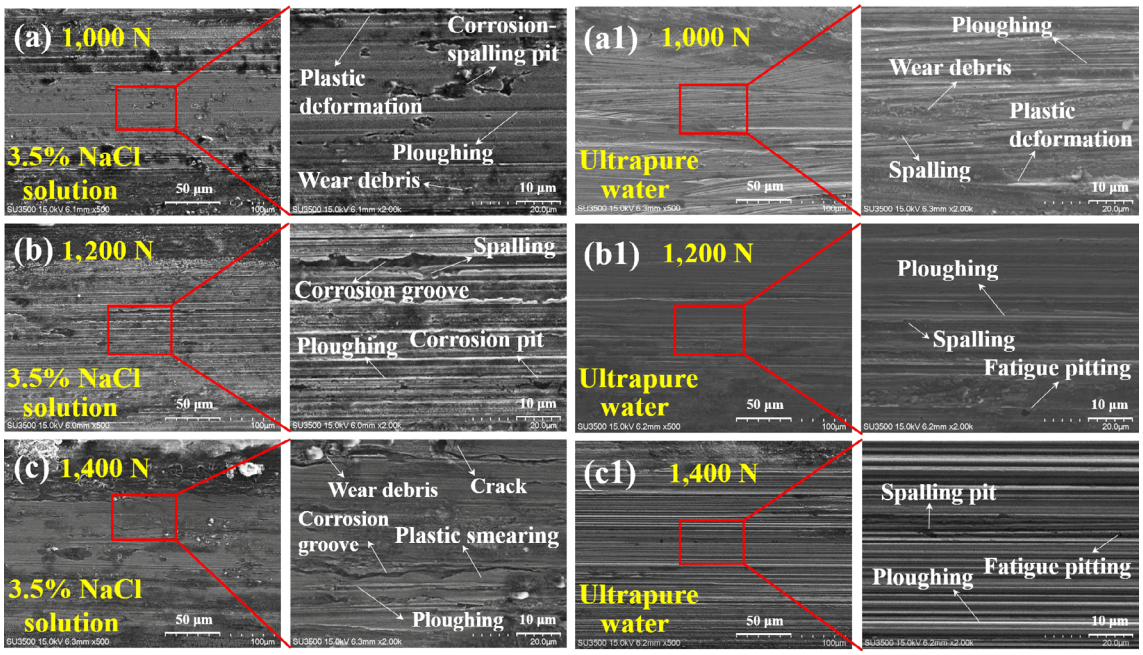

Fig. 5 Wear morphologies of fatigue wires when subjected to different fatigue loads at the fatigue cycles of 2×10^5.

cycles of 1×10^4, there is obvious material cracking on the edge of the wear marks, and the cracks are small and dense. The primary factor contributing to this is the comparatively elevated surface hardness of the galvanized coating on the fatigue wire. Under the alternating tensile stress, cracks occur on the wire surface. Meanwhile, the participation of the corrosive medium increases the risk of cracking of the galvanized coating. The relative sliding causes the decreasing number of cracks in the wear area. The surface micro-convex body has plastic deformation, forming a tiny welding contact point. When the wires slide relatively to each other, the points formed by the adhesion effect are sheared, falling off into wear debris. These abrasive particles continue to roll and slide across the surface, resulting in the spalling and adhesion of material, or migration from one surface to another. The surface cracks are fine and shallow, so they are covered or removed. The obvious groove-like wear marks observed in the worn region are primarily caused by the normal force exerting pressure on the wire surface, resulting in the plowing of hard bulges or rough peaks. This pressure leads to plastic deformation, which in turn expels the flaky or scale-like spalling debris. Moreover, the tangential force induces shearing, plowing, and cutting of the wire surface by the abrasive particles, leading to the detachment of surface material. As shown in Fig. 4(b), the decreasing grooves and ploughings, the increasing corrosion pits, the accumulation and adhesion of debris and pits of varying sizes appear on the worn surface. Under the influence of alternating tensile stress, the portion of abrasive particles subjected to the corrosive medium becomes loose and gets embedded into the wire surface. The shallow and wide indentation is produced on the surface, which is then plowed along the sliding direction to produce grooves of different depths. The wear mark compresses the remaining abrasives towards its periphery, resulting in the accumulation and adhesion. Corrosion prompts the expansion of the initial surface crack towards the interior, while a secondary crack develops and bends to the surface. The tensile stress causes the cracks to break off and form a fan-shaped pit. The variation in size of surface cracks results in varying spalling areas of the surface material. At the fatigue cycles of 1×10^5, there is a significant decrease in the zinc content on the worn surface, plummeting from 94.26% to 6.61% (Fig. S1 and Table S1, shown in ESM). The worn surface loses the protection of galvanized coating, resulting in more significant corrosion phenomenon. Figure 4(c) shows the dense and deep corrosion pits, a large amount of debris accumulation, and wide and long cracks perpendicular to the sliding direction.

As the fatigue cycle continues to increase, the zinc content on the worn surface continues to decrease to ~2.3% and is relatively stable, indicating a basic depletion of the galvanized coating. The primary source of the small amount of zinc originates from the introduction of wear debris at the wear mark's edge. This occurrence is attributed to the friction between galvanized steel wires, which leads to the destruction of the newly applied zinc coating on the edges of the upper and lower parallel steel wires during continuous wear. Reciprocating sliding pushes the flaking debris into the wear zone. As shown in Figs. 4(d) and 4(e), there are many large cracks, multiple spalling pits and a large amount of debris and abrasive particles accumulated. The progressive enlargement of small surface pitting and cracks ultimately leads to the formation of larger cracks and corrosion pits. Ploughing phenomenon is weakened. Material adhesion and spalling are increased. The primary reason behind this phenomenon is the direct result of an increased number of fatigue cycles, which prolongs the exposure time of the alternating tensile stress on the fatigue wire, as well as the duration of exposure to the corrosive medium. Meanwhile, the impact of the temperature rise effect induced by friction is heightened [14, 33], resulting in an activating effect on Cl^-. Therefore, the increasing fatigue cycles enhance the characteristics of adhesive wear, fatigue wear and corrosion wear, while weaken the abrasive wear gradually.

From Fig. 5, there are obvious ploughings, plastic deformation, small cracks, corrosion pits, adhesion flaking, and fatigue spalling under different fatigue loads at the fatigue cycles of 2×10^5. As the fatigue load increases, the impact of corrosive medium intensifies, creating a synergistic relationship between corrosion and fatigue. Due to the combined influence of tensile stress and corrosive medium, the surface cracks undergo continuous expansion. Then, the relative sliding causes the material spalling, forming the different sizes of spalling pits. Cl^- in the solution accumulates in the pits, continuously eroding the surface. As a result, the spalling pits grow, forming long, narrow and deep pits (Figs. 5(b) and 5(c)). At the fatigue load range of 750–1,000 N, the corrosion pits, fatigue spalling pits and adhesive flaking pits are more obvious than that of other fatigue loads. The primary cause is attributed to the low fatigue load, which results in the minor adhesion and debris accumulation, and the pits are not covered in the process of relative sliding. However, the material adhesion covers part of the pits under high fatigue load. Hence, the predominant wear mechanisms observed under different fatigue loads in 3.5% NaCl solution include adhesive wear, abrasive wear, fatigue wear, and corrosion wear. As the fatigue load increases, the fatigue wear, adhesive wear and corrosion wear gain prominence, whereas abrasive wear exhibits a diminished influence. As shown in Figs. 5(a1)–5(c1), the worn surface exhibits obvious smear, fine cracks, ploughings, abrasive particles, and material accumulation at the fatigue load range of 750–1,000 N in ultrapure water. There are several directions of wear marks, which may be attributed to the small compression stress under low load, the abrasive particles can break free and roll or slide between contact surface in different direction. Under the tensile stress, the wear particles leave scratches that are not completely consistent with the sliding direction. The wear marks on the worn surface intensify in the sliding direction with the increasing fatigue load, accompanied by noticeable debris accumulation and the formation of fan-shaped pits resulting from fatigue spalling. At the fatigue load range of 750–1,400 N, the dense and deep ploughings on the worn surface are particularly significant, and the pitting are obvious. Consequently, when subjected to varying fatigue loads in ultrapure water, the predominant wear mechanisms include adhesive wear, abrasive wear, and fatigue wear. In addition, as the fatigue load increases, the characteristics of abrasive wear and fatigue wear are more significant, and the characteristics of adhesive wear are weakened.

3.3 Wear profile and cross-sectional failure area

The wire's wear mark is a long and narrow rectangle, and the wear width increases with the increase of fatigue cycles at the fatigue load range of 750–1,400 N (Fig. S2 in the ESM and Fig. 6(a)). The wear width increases by 192.6% from 121.5 to 355.5 μm. The growth rates of wear width are 34.0%, 33.1%, 31.5% and 24.8%, respectively, showing a decreasing trend.

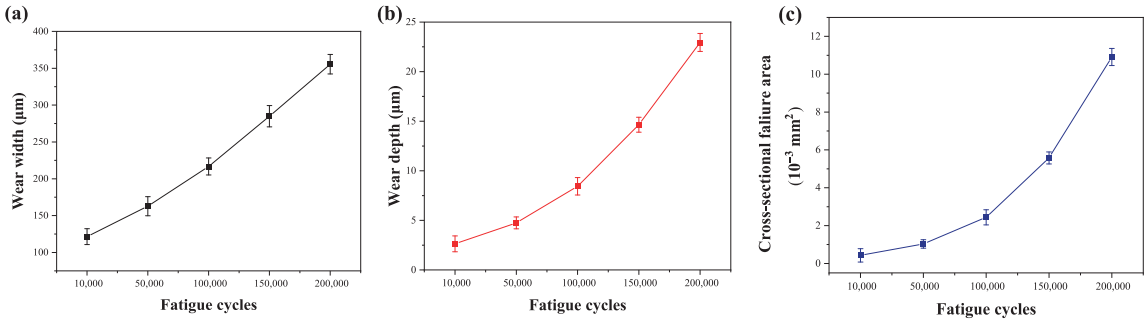

Fig. 6 Wear profile of fatigue wire when subjected to different fatigue cycles at the fatigue load range of 750–1,400 N: (a) wear width, (b) wear depth, and (c) cross-sectional failure area.

This is mainly because the roughness of the wire surface is relatively large at the early wear stage, and the abrasive wear is serious (Figs. 4(a) and 4(b)). The corrosion of wire contact surface enhances with the increasing fatigue cycles, the adhesion increases, and the surface plow cutting decreases (Figs. 4(c)–4(e)). Figures 6(b) and 6(c) show the wires' wear depth and cross-sectional failure area increase with the increase of fatigue cycle with the approximate parabola at the fatigue load range of 750–1,400 N. The reason of their evolutions is the same as the wear width. The wear depth increases from 2.64 to 22.94 μm, which is 8.69 times as much as that of 1×10^4 cycles. The wire's cross-sectional failure area increases by 25.5 times from 4.28×10^{-4} to 1.09×10^{-2} mm^2, and the increase is more obvious due to the presence of two contact surfaces between the fatigue wire and the contact wires.

As shown in Figs. 7 and 8(a), the wear width in different mediums increases with the increase of fatigue load at the fatigue cycles of 2×10^5. Upon increasing the maximum fatigue load from 1,000 to 1,200 N, the rate of increase is found to be 16.1% in ultrapure water and 17.7% in 3.5% NaCl solution. When the maximum fatigue load increases from 1,200 to 1,400 N, the wear width demonstrates a respective increase of 22.0% in ultrapure water and 55.5% in 3.5% NaCl solution. Under low fatigue load, there is little difference in the rate of wear width increase between 3.5% NaCl solution and ultrapure water as compared to a significant difference under high fatigue load. These illustrate that Cl^- has little impact on wear under low fatigue load, while the coupling effects of fatigue and corrosion have a significant influence on wear under high fatigue load. This may be because the low fatigue load makes it difficult to destroy the surface passivation film in corrosive medium, which plays a certain protective role on wear. The high fatigue load makes the anti-fatigue performance of steel wire decline rapidly, the contact surface is more prone to producing fatigue spalling (wear morphologies have been analyzed in Section 3.2). The corrosive medium gathers on the spalling surface, further erodes the surface, resulting in material removal under the tensile stress, and enhancing the wear. The ultrapure water functions solely as a lubricant. The incremental impact of fatigue load on wear width remains relatively consistent, suggesting

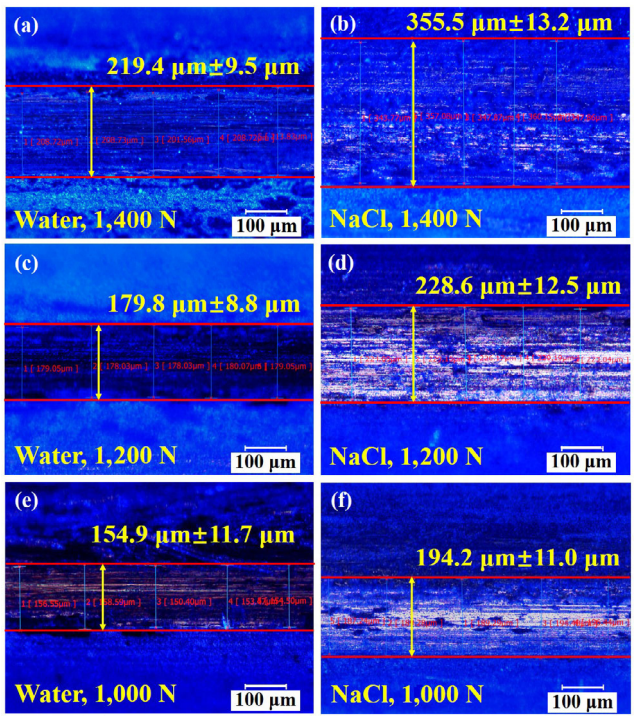

Fig. 7 Wear width morphologies of fatigue wires when subjected to different fatigue loads at the fatigue cycles of 2×10^5.

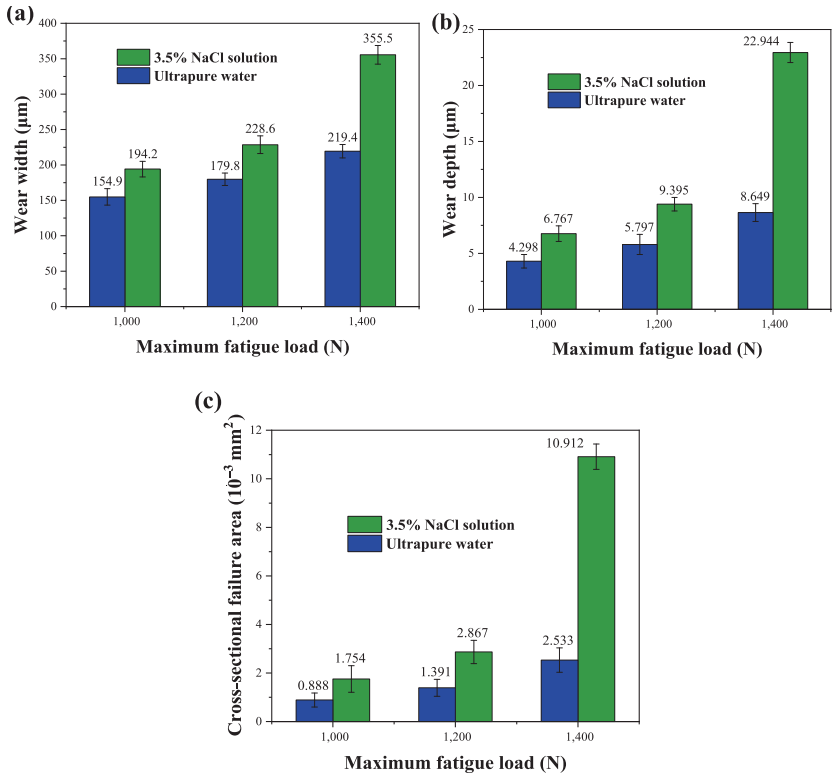

Fig. 8 Wear profile of fatigue wire when subjected to different fatigue loads at the fatigue cycles of 2×10^5: (a) wear width, (b) wear depth, and (c) cross-sectional failure area.

a stable influence of water on wear. From Fig. 8(b), the wear depth of the fatigue wire exhibits an increase with the increasing fatigue load, demonstrating a notable difference between 3.5% NaCl solution and ultrapure water. In the corrosive medium, with the maximum fatigue load going from 1,000 to 1,400 N, the wear depth of fatigue wire increases by 38.83% and 144.30% as compared to 34.88% and 49.20% in ultrapure water. Similarly, when the maximum fatigue load increases from 1,000 to 1,200 N, the cross-sectional failure area in ultrapure water and 3.5% NaCl solution increases by the same amplitude (about 1.6 times). When the maximum fatigue load continues to increase to 1,400 N, the increase of failure area in ultrapure water changes slightly as compared to a significant increase by 280.61% in the corrosive medium (Fig. 8(c)). These demonstrate that high fatigue load induces the decreasing anti-fatigue properties and enhance the effect of corrosion on wear in 3.5% NaCl solution.

3.4 Volume loss and wear rate

The wire's total volume loss increases in parabolic shape as the fatigue cycle increases at the fatigue load range of 750–1,400 N. It increases by 25.38 times from 0.026 mm^3 to 0.660 mm^3 (Fig. 9(a)). As shown in Fig. 9(b), the wear rate is measured to be 0.056 mm^3/h at 1×10^4 cycles. The minimum wear rate is 0.027 mm^3/h at the 5×10^4 cycles. Then, it gradually increases to 0.071 mm^3/h with the increasing cycle. The initial wear rate is relatively high, which can be inferred from the wear morphologies in Fig. 4. The abrasive wear plays a major role in strengthening the wear. When the abrasive debris are removed gradually, the roughness of the wire surface decreases, leading to the decrease in the wear rate. Then, corrosion has a significant impact on material loss as the fatigue cycles increase. The quantitative characterization and analysis of tribo-corrosion-fatigue interaction will show in Section 3.6. Therefore, the wear is increasing, and the wear rate increases gradually.

From Fig. 10(a), the wire's total volume loss in different mediums increases exponentially as the fatigue load increases at the fatigue cycles of 2×10^5. The maximum fatigue load escalates from 1,000 to 1,400 N, the total volume loss is 1.63 times and

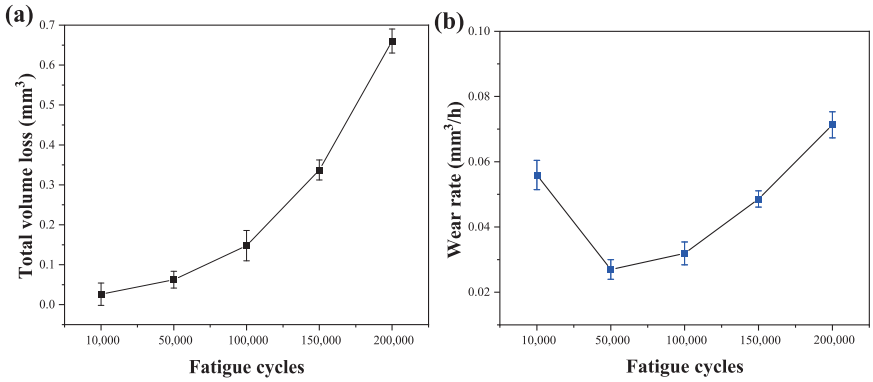

Fig. 9 (a) Total volume loss and (b) wear rate when subjected to different fatigue cycles at the fatigue load range of 750–1,400 N.

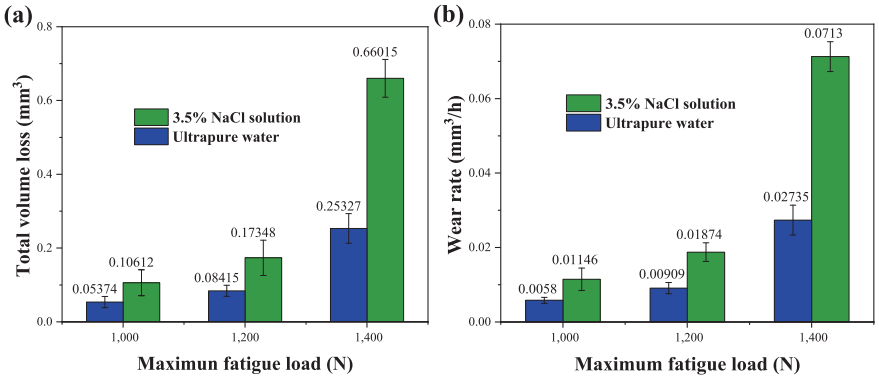

Fig. 10 (a) Total volume loss and (b) wear rate when subjected to different fatigue loads at the fatigue cycles of 2×10^5.

3.81 times of the former in 3.5% NaCl solution as compared to 1.57 times and 3.01 times in ultrapure water. The total volume loss in the corrosion solution demonstrates a more rapid growth rate compared to ultrapure water. The greater the fatigue load is, the faster the growth is, which is attributed to the enhancement of corrosion. At the maximum fatigue loads of 1,000, 1,200 and 1,400 N, the wire's total volume loss in 3.5% NaCl solution exceeds that in ultrapure water by factors of 1.97, 2.06 and 2.61, respectively. The total volume loss, wear width, wear depth, and cross-sectional failure area exhibit similar evolutionary patterns due to a shared underlying cause. Figure 10(b) illustrates that the wire's wear rate increases with the increase of fatigue load at 2×10^5 cycles, aligning with the observed trends in total volume loss. The severity of wear intensifies with higher fatigue loads, resulting in faster total volume loss.

3.5 Electrochemical corrosion resistance

The Nyquist diagrams are subjected to analysis and fitted using the *R(Q(R(QR))* equivalent circuit (Fig. 11(a)). This circuit comprises various components, where *Rs* represents the resistance of the corrosion solution, *CPE*1 denotes the capacitance of the surface passivation film on the main cable wire, *Rt* represents the resistance of the surface passivation film, *CPE*2 represents the double layer capacitance between the wire substrate and the passivation film, and *Rf* signifies the charge transfer resistance. The equivalent circuit parameters of the main cable wires under different fatigue loads at the fatigue cycles of 2×10^5 are shown in Table S3 in the ESM. Figure S3 in the ESM reveals that the wire subjected to tribo-corrosion-fatigue coupling damage has the worst corrosion resistance. When worn in 3.5% NaCl solution, the arc radius of the surface capacitive reactance of the fatigue wire decreases as the fatigue load increases. This reduction indicates a decline in the corrosion resistance of the fatigue wire. The underlying cause can be attributed to the concentration of stress within the wire due to the increasing fatigue load. Consequently, the surface material of the fatigue wire is more prone to cracking

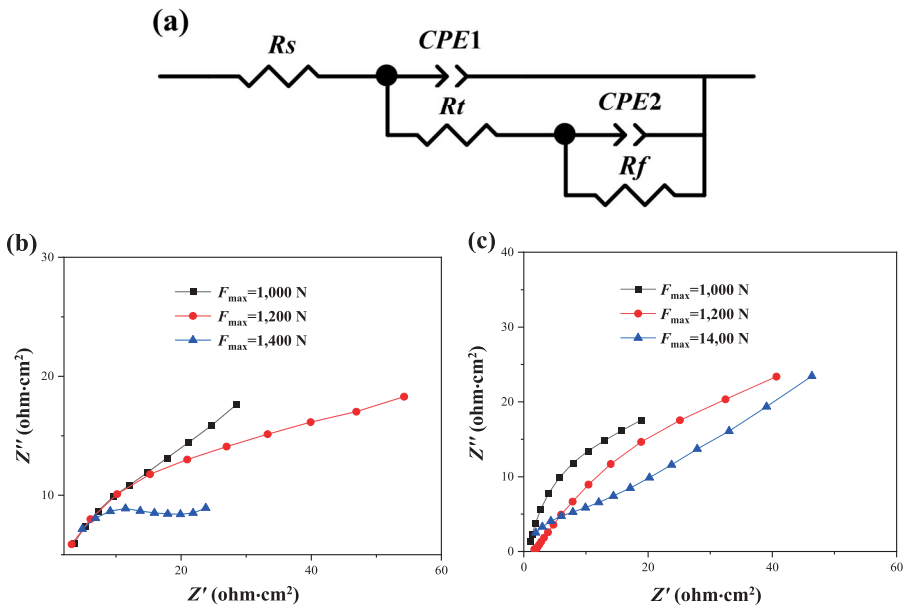

Fig. 11 (a) Equivalent circuit, Nyquist diagrams of fatigue wire when subjected to different fatigue loads at the fatigue cycles of 2×10^5 in (b) 3.5% NaCl solution and (c) ultrapure water (Note: Z″and Z′ in the diagrams are the imaginary part and the real part of the impedance, respectively)

or deformation, leading to material spalling on the wire's surface. This spalling is then removed through relative sliding, exacerbating the corrosion effects. Cl^- in corrosion solution accumulates and sticks in these spalling pits, constantly eroding the surface. In addition, when exposed to prolonged fatigue loading, the surface hardness of the fatigue wire may decrease, rendering it more susceptible to wear. Then, the presence of corrosive mediums further increases the susceptibility of the wire surface to corrosion. The wire surface experiences a reduction in corrosion resistance. In ultrapure water, the arc radius of the surface capacitive reactance for the worn fatigue wire follows a similar trend to that observed in 3.5% NaCl solution (Fig. 11(c) vs. Fig. 11(b)). This similarity arises due to the concentration of internal stress as the fatigue load increases. The wire surface is more likely to flake and form wear debris. Friction forces the abrasive particles to plow the surface, which leads to the constant wear. The ploughing phenomenon becomes more pronounced with higher fatigue loads (Figs. 5(a1)–5(c1)), indicating more severe wear. Therefore, as the fatigue load increases, the wire surface is more prone to being corroded, the corrosion resistance decreases. Comparing the Nyquist diagrams between 3.5% NaCl solution and ultrapure water reveals that the arc radius of the capacitive reactance is greater in ultrapure water. These results suggest that the surface corrosion resistance of the fatigue wire is better in ultrapure water compared to 3.5% NaCl solution. This discrepancy can be attributed to the intensified damage and material destruction caused by the corrosive medium, where corrosion and wear mutually reinforce each other. In 3.5% NaCl solution, the material defects of the surface increase and continuously migrate inward due to the erosion of Cl^- on the wire surface. The metal loses electrons into the electrolyte solution to form a galvanic cell. Electrochemical reactions occur and constantly destroy the wire surface, resulting in a loose and porous surface with relatively easy interfacial charge transfer. In ultrapure water, the fatigue wire only exhibits tribo-fatigue behaviors. There is no electrolyte in the water, the galvanic cell cannot be formed, the electrochemical reaction cannot take place. The predominant surface wear mechanisms observed in the fatigue wire are fatigue wear and abrasive wear (Fig. 5), resulting in the relatively few surface defects as compared to that in 3.5% NaCl solution. The ability of metal to lose electrons is relatively weak, and the charge transfer is difficult. Therefore, under the same fatigue load, the impedance

arcs show smaller radii in 3.5% NaCl solution when compared to larger radii observed in ultrapure water.

Figure 12 shows that the Tafel polarization curves of fatigue wires in different mediums exhibit a leftward shift as the fatigue load increases at the fatigue cycles of 2×10^5. In the corrosion solution, the corrosion potential decreases from −1.312 to −1.340 V as the maximum fatigue load increases from 1,000 to 1,400 N, and the density of the corrosion current increases from 3.970×10^{-4} to 5.480×10^{-4} A·cm^{-2} (Table 1). The decrease in corrosion potential, coupled with the increase in corrosion current density, implies a reduction in the surface corrosion resistance of the fatigue wire. This phenomenon mirrors the observation of the decreasing arc radius of capacitive reactance with increasing fatigue load. The influence of corrosive medium on worn surfaces is enhanced. In ultrapure water, with an increase in the maximum fatigue load from 1,000 to 1,400 N, the corrosion potential experiences a decrease from −1.314 to −1.350 V, while the density of corrosion current increases from 3.811×10^{-4} to 5.395×10^{-4} A·cm^{-2} (Table 1). These results signify a decrease in the surface corrosion resistance of the worn wire, rendering it more susceptible to corrosion, similar to the observations made in 3.5% NaCl solution. This can be attributed to the heightened significance of abrasive wear characteristics accompanying the increasing fatigue load, resulting in increased surface roughness, intensified wear, and enhanced corrosion effects. By comparing the Tafel data in two mediums, it can be found that the corrosion potential in 3.5% NaCl solution is slightly higher than that in ultrapure water. This could be attributed to the passivation of the worn surface of the fatigue wire in 3.5% NaCl solution, providing a certain level of surface protection. Furthermore, the worn area in 3.5% NaCl solution is notably larger than that in ultrapure water, leading to a slightly higher corrosion potential. Therefore, the corrosion current densities in two mediums are focused on. Under different fatigue loads, the corrosion current density in 3.5% NaCl solution consistently exceeds that in ultrapure water, aligning with the lower impedance observed in the former. These pieces of evidence collectively indicate that the corrosion resistance of the fatigue wire, coupled with the tribo-corrosion-fatigue damage, is comparatively weaker.

3.6 Tribo-corrosion-fatigue interaction

The fatigue wire is subjected to the alternating tensile stress, which leads to the unbalanced stress transmission due to the uneven internal structure,

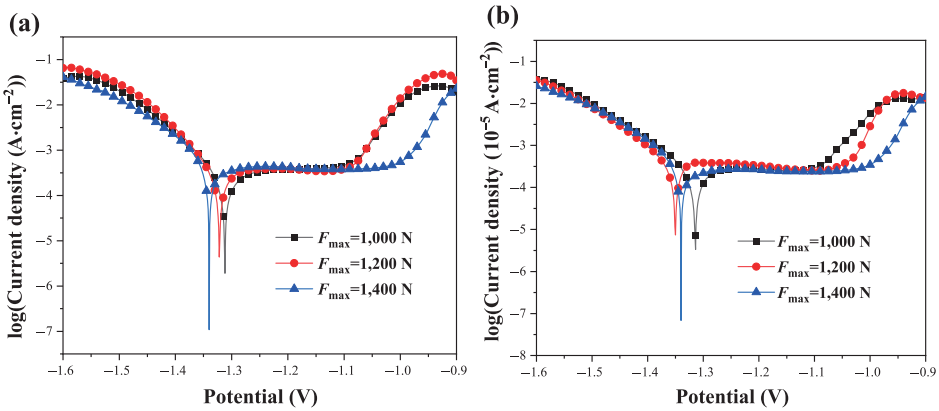

Fig. 12 Potentiodynamic polarization curves of fatigue wire when subjected to different fatigue loads at the fatigue cycles of 2×10^5 in (a) 3.5% NaCl solution and (b) ultrapure water.

Table 1 Test results of potentiodynamic polarization curves of fatigue wires worn in different mediums.

F_{max} (N)	1,400		1,200		1,000	
	Water	NaCl	Water	NaCl	Water	NaCl
E_{corr} (V)	–1.346	–1.34	–1.350	–1.322	–1.314	–1.312
i_{corr} (10^{-4} A·cm^{-2})	5.395	5.480	4.652	4.781	3.811	3.970

and some areas develop into stress concentration areas. At the same time, there are many tiny cracks in the internal defects of the wire. The continuous fatigue load makes the cracks propagate continuously. The stress transmission is hindered, and the fatigue failure is aggravated. The contact surface of the parallel wires is subjected to alternating compressive stress and tensile stress, resulting in the wear due to the relative sliding. In corrosive medium, Cl^- possesses a small radius and exhibits strong penetration ability [20, 34], leading to the erosion of the wire surface and subsequent corrosion damage. In the actual service condition of the main cable, fatigue, friction, and corrosion of the parallel wires interact and promote each other. The interaction mechanism diagram of tribo-corrosion-fatigue in 3.5% NaCl solution is shown in Fig. 13. The fatigue-induced spalling of surface material enlarges the contact area between the material and the corrosive medium, thereby intensifying the corrosive effect. The spalling is removed with the relative sliding. Cl^- from the corrosion solution absorbs on the wire surface and into the substrate, constantly diffusing and gathering at the defect. In this context, the initiation of fatigue cracks takes place, and the presence of corrosion promotes material dissolution, ultimately accelerating the growth rate of the fatigue crack. The material is relatively easy to flake with the relative sliding, accelerating the loss of the material. The friction constantly increases the material defects, the points of fatigue crack initiation increase. The friction and wear cause the surface material to becomes uneven, exposing more fresh surface. The fresh surface exhibits higher reactivity compared to other regions, making it susceptible to localized corrosion and dissolution in the presence of corrosive mediums. Moreover, the interplay between friction, corrosion, and fatigue creates a coupling effect, resulting in intricate alterations in material properties. Corrosion induces changes in the chemical composition of the wire surface, subsequently influencing its mechanical properties and wear characteristics.

In this study, the interplay of the tribo-corrosion-fatigue damage ultimately culminates in the volume loss of the fatigue wire. As described in previous studies [20, 34], V is the sum of the pure corrosion-induced volume loss (V_{corr}), V_{wear} and the volume loss resulting from the tribo-corrosion-fatigue interaction (ΔV). ΔV consists of the volume loss promoted by wear affecting corrosion (V_{wc}) and the volume loss promoted by corrosion affecting wear (V_{cw}). The V can be described by the sum of V_{corr}, V_{wear}, V_{wc}, and V_{cw}. The total wear-induced volume loss (ΔV_{wear}) is composed of V_{wear} and V_{cw}. The total corrosion-induced volume (ΔV_{corr}) is divided into V_{corr} and V_{wc}. To determine V and V_{wear}, the method outlined in Section 2.3 is employed. The prolonged testing period, the presence of a long fatigue wire, and the contact between the fatigue wire and the contact wire (connected to the fixture) in the etching bath contribute to a complex resistance composition within

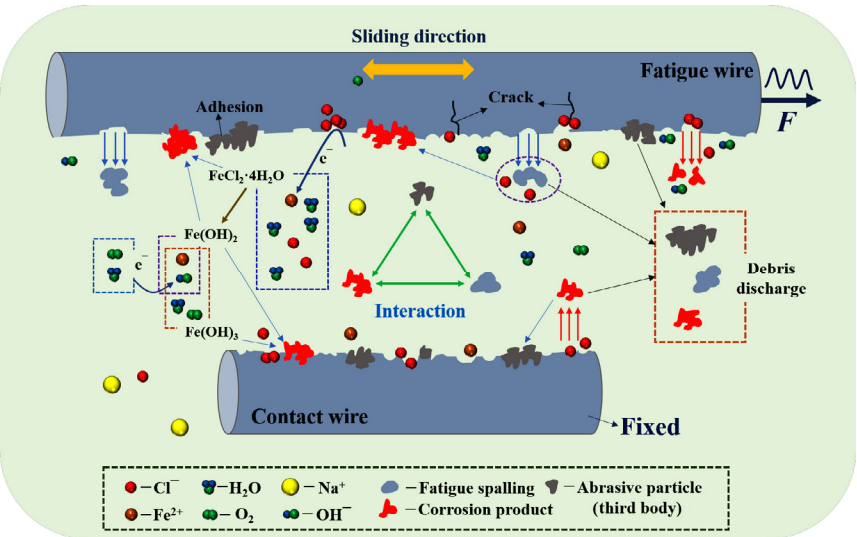

Fig. 13 Interaction mechanism diagram of tribo-corrosion-fatigue of microsegment wire in 3.5% NaCl solution.

the corrosion circuit. Directly measuring the corrosion current of the fatigue wire is challenging due to these factors. Hence, following the bending tribo-corrosion-fatigue test, a Tafel polarization curve is immediately measured for a specific length of the worn wire to obtain the corrosion current density value. This value is then converted to determine the corrosion current (I) for the entire worn wire [35]. To be specific, the corrosion current density of the test section is used to characterize the corrosion current density of the whole section of worn steel wire due to the similar corrosion level across the entire wire. The corrosion current of the fatigue wire can be determined by multiplying it with the wear area of the wire. The corrosion current of the wire under static corrosion conditions, in the absence of wear, is referred to as the pure corrosion current (I_c). V_{corr} and V_{wc} can be calculated by Eqs. (6) and (7) [36, 37].

$$V_{corr} = \frac{I_c W t}{F n \rho} \tag{6}$$

$$V_{wc} = \frac{W(I - I_c)t}{F n \rho} \tag{7}$$

where, t represents the duration of the tribo-corrosion-fatigue test. F corresponds to the Faraday constant with a value of 96,500 C·mol^{-1}. The density of the wire is denoted as ρ. The relative atomic mass (W) is calculated based on the composition of the worn surface. The parameter n signifies the number of electron transfers. At 2×10^5 cycles, the worn surface of the wire contains about Fe of 90% and the Zn of 2%–3% (Table S1 in the ESM), so the final W is 52.5. Iron and zinc both lose two electrons in the electrochemical reaction, so n is 2.

As shown in Table 2 and Fig. 14(a), all components of volume loss exhibit an upward trend as the fatigue load increases at the fatigue cycles of 2×10^5. The magnitude of this increase becomes more pronounced with higher fatigue loads. This is attributed to the fact that the increasing fatigue load puts more stress on the wire, and the increase of stress leads to the

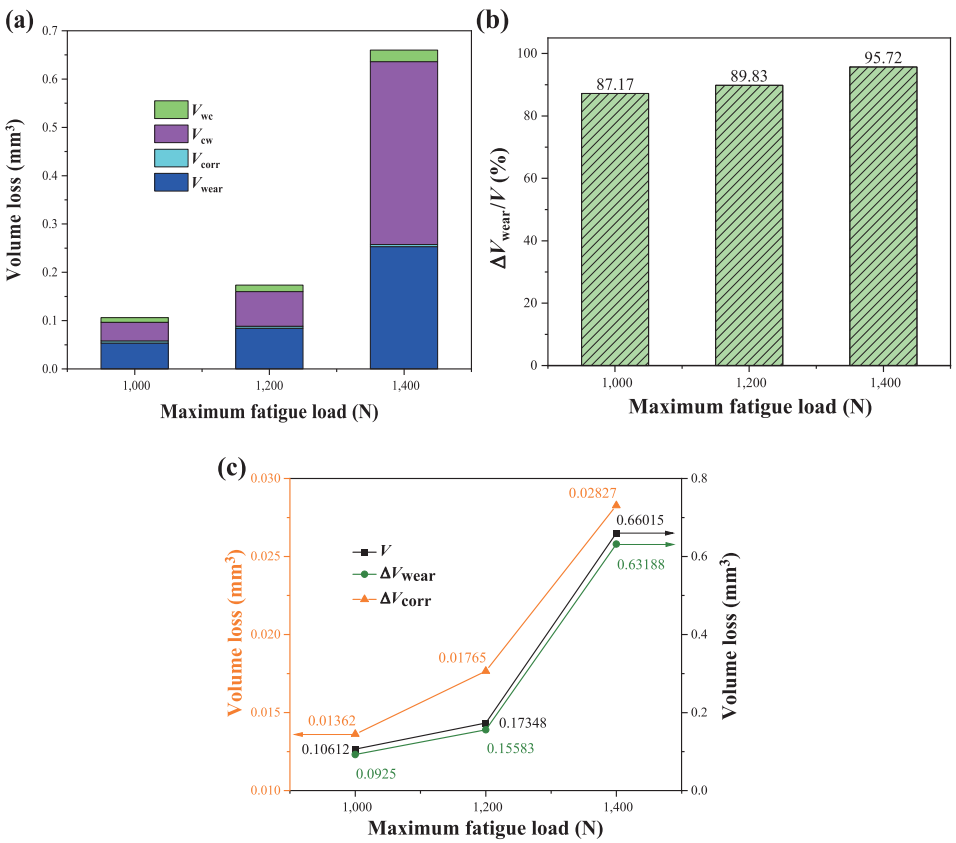

Fig. 14 Diagrams depicting the relationship between volume loss components of fatigue wire when subjected to different fatigue loads at the fatigue cycles of 2×10^5.

Table 2 Volume loss components of cable wires when subjected to different fatigue loads at 2×10^5 cycles.

Maximum fatigue load (N)	V (mm^3)	V_{wear} (mm^3)	V_{corr} (mm^3)	V_{wc} (mm^3)	V_{cw} (mm^3)	V_{cw}/V (%)	$\Delta V/V$ (%)
1,400	0.66015	0.25327	0.00421	0.02406	0.37861	57.35	61.00
1,200	0.17348	0.08415	0.00421	0.01344	0.07168	41.32	49.07
1,000	0.10612	0.05374	0.00421	0.00941	0.03876	36.52	45.39

increasing pressure on the contact surface. The wire's fatigue resistance decreases after being subjected to the repeated stress loading. The small cracks on the wire's worn surface gradually expand, leading to spalling and removal under the relative sliding. As shown in Figs. 14(b) and 14(c), ΔV_{wear} and V have very small difference, and ΔV_{wear} accounts for 87.17%, 89.83%, and 95.72% at the maximum fatigue loads of 1,000, 1,200 and 1,400 N, respectively. The increasing proportion can be attributed to the increase of fatigue load, which accelerates the initiation and propagation of cracks, resulting in easy material spalling and increasing the wear rate (Fig. 10(b)). Therefore, the V_{wear} increases. In addition, the high fatigue load produces greater temperature rise effect [38], which activates the corrosive medium, thereby enhancing the corrosion on the worn surface. The V_{cw} increases. The ΔV_{corr} exhibits an increase as the fatigue load increases, while at a lower rate compared to V_{wear}, so the proportion in the V falls. Figure 15 shows the proportions of the ΔV in the V are 45.39%, 49.07% and 61.00% at the maximum fatigue loads of 1,000, 1,200, and 1,400 N, respectively, at 2×10^5 cycles. This finding indicates the significant impact of interaction on volume loss during tribo-corrosion-fatigue behaviors, underscoring its indispensability. The interaction is enhanced by the increase of fatigue load. Cl^- from the corrosive medium accumulates and adheres to the worn surface, constantly eroding the wire substrate, thereby promoting the wear.

The value of V_{wc}/V_{cw} is an important parameter to quantitatively characterize the extent of the interaction [20, 22]. When V_{wc} or V_{cw} value is negative, it indicates a reciprocal inhibition relationship between corrosion and wear, whereas when both values are positive, the relationship becomes mutually reinforcing. V_{wc}/V_{cw} ranging from 0 to 0.1 represents synergy, where corrosion predominantly enhances wear. V_{wc}/V_{cw} ranging from 0.1 to 1 is the synergy and additive

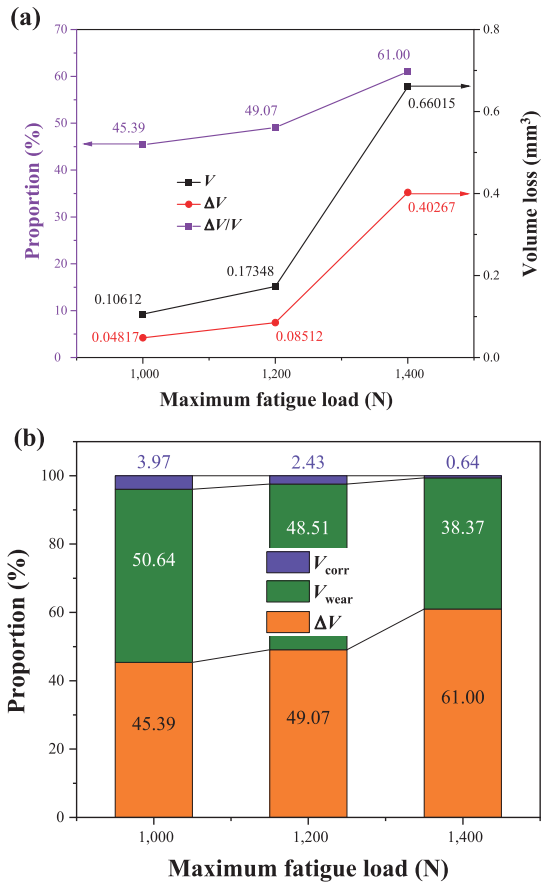

Fig. 15 Proportion of interaction and volume loss components of fatigue wire when subjected to different fatigue loads at the fatigue cycles of 2×10^5.

effect, in which wear is also important in promoting corrosion. As shown in Fig. 16, both V_{wc} and V_{cw} exhibit positive values, signifying a mutually reinforcing relationship between corrosion and wear. The values decrease as the fatigue load increases, revealing the increasing promoting effect of corrosion on wear. The V_{wc}/V_{cw} value ranges from 0 to 0.1 at the fatigue load range of 750–1,400 N, suggesting synergy and highlighting corrosion as the primary driver of wear. The V_{wc}/V_{cw} value ranges from 0.1 to 1 at the maximum fatigue load of 1,000 N and 1,200 N, indicating that interaction is in the synergy and additive effect zone.

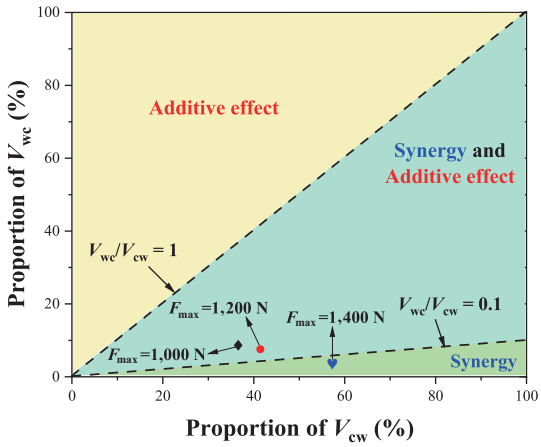

Fig. 16 V_{wc}/V_{cw} when subjected to different fatigue loads at 2×10^5 cycles.

In this case, the difference between the V_{wc} and V_{cw} is small, and the contribution of corrosion to wear is just as significant as the contribution of wear to corrosion. This may be because the wear degree is weak under low fatigue load as compared to severe under high fatigue load, and the promotion of corrosion to wear is not significant. These can be obtained from wear morphologies and volume loss analysis under different fatigue loads.

4 Conclusions

In this paper, a self-made wire test rig was employed to investigate the effect of fatigue load on the bending tribo-corrosion-fatigue behaviors between the parallel wires of a suspension bridge's main cable. The tribological and electrochemical corrosion properties of fatigue wires in different mediums is revealed qualitatively and quantitatively. The interaction between the friction, corrosion, and fatigue is quantitatively characterized and analyzed in detail. The conclusions obtained are as follows.

1) The friction coefficient between the main cable wires is found to be higher in ultrapure water compared to 3.5% NaCl solution, and it decreases as the fatigue load increases. The wear width, wear depth, cross-sectional failure area, total volume loss, and wear rate all exhibit an upward trend with the increasing fatigue load, with significantly greater values observed in 3.5% NaCl solution as compared to ultrapure water.

2) The main wear mechanisms in 3.5% NaCl solution are adhesive wear, abrasive wear, fatigue wear, and corrosion wear as compared to adhesive wear, abrasive wear, and fatigue wear in ultrapure water.

3) With the increase of fatigue load, the corrosion resistance in 3.5% NaCl solution decreases and proves to be inferior to that in ultrapure water.

4) As the fatigue load increases, the tribo-corrosion-fatigue interaction gains greater significance, leading to an increase in its influence. The volume loss attributed to this interaction ranges from 45% to 61% of the total volume loss observed.

Acknowledgements

The research received funding from the National Natural Science Foundation of China (Grant Nos. 52175205 and 51875565) and the Chinese Postdoctoral Science Foundation (Grant Nos. 2019M652001 and 2020T130695). The authors express their gratitude to the Top-notch Academic Programs Project of Jiangsu Higher Education Institutions (TAPP) and a Project Funded by the Priority Academic Program Development of Jiangsu Higher Education Institutions (PAPD).

Declaration of competing interest

The authors have no competing interests to declare that are relevant to the content of this article. The author Dagang WANG is the Youth Editorial Board Member of this journal.

Electronic Supplementary Material: Supplementary material is available in the online version of this article at https://doi.org/10.1007/s40544-023-0830-y.

References

[1] Wang D G, Ye J H, Wang B, Abdel Wahab M. Review on the service safety assessment of main cable of long span multi-tower suspension bridge. *Appl Sci* **11**(13): 5920 (2021)

[2] Chong H L, Wang D G, Wang B, Shen X M, Abdel Wahab M. Gradual deterioration behavior of the load-bearing strength of main cable wires in a suspension bridge. *Appl Sci* **13**(1): 129 (2022)

[3] Wang S Q, Wan X, Guo M H, Qiao H, Zhang N, Ye Q. Nonlinear dynamic analysis of the wind–train–bridge system of a long-span railway suspension truss bridge. *Buildings* **13**(2): 277 (2023)

[4] Wang D G, Zhu H L, Gao W L, Zhang D K, Tan D L, Zhao X. Research on dynamic contact and slip mechanisms of parallel steel wires in the main cable of suspension bridge. *J Mech Eng* **57**(11): 228 (2021)

[5] Karanci E, Betti R. Modeling corrosion in suspension bridge main cables. I: Annual corrosion rate. *J Bridge Eng* **23**(6) 04018025 (2018)

[6] Karanci E, Betti R. Modeling corrosion in suspension bridge main cables. II: Long-term corrosion and remaining strength. *J Bridge Eng* **23**(6): 04018026 (2018)

[7] Wang S J, Khatir S, Abdel Wahab M. Proper orthogonal decomposition for the prediction of fretting wear characteristics. *Tribol Int* **152**: 106545 (2020)

[8] Zhang J, Wang D G, Song D Z, Zhang D K, Zhang C L, Wang D A, Araújo J A. Tribo-fatigue behaviors of steel wire rope under bending fatigue with the variable tension. *Wear* **428–429**: 154–161 (2019)

[9] Chen Y P, Meng F M, Gong X S. Interwire wear and its influence on contact behavior of wire rope strand subjected to cyclic bending load. *Wear* **368–369**: 470–484 (2016)

[10] Li H Y, Ren Z Y, Su X L, Shen L L, Huang J M. Study on the fretting wear evolution model of wires with curvature inside metal rubber. *Tribol Lett* **71**(1): 22 (2023)

[11] Wang D G, Li X W, Wang X R, Zhang D K, Wang D A. Dynamic wear evolution and crack propagation behaviors of steel wires during fretting-fatigue. *Tribol Int* **101**: 348–355 (2016)

[12] Shen Y, Zhang D K, Duan J J, Wang D G. Fretting wear behaviors of steel wires under friction-increasing grease conditions. *Tribol Int* **44**(11): 1511–1517 (2011)

[13] Peng Y X, Huang K, Ma C B, Zhu Z C, Chang X D, Lu H, Zhang Q, Xu C M. Friction and wear of multiple steel wires in a wire rope. *Friction* **11**(5): 763–784 (2023)

[14] Chang X D, Huang H B, Peng Y X, Li S X. Friction, wear and residual strength properties of steel wire rope with different corrosion types. *Wear* **458–459**: 203425 (2020)

[15] Wang D G, Song D Z, Wang X R, Zhang D K, Zhang C L, Wang D A, Araújo J A. Tribo-fatigue behaviors of steel wires under coupled tension-torsion in different environmental media. *Wear* **420–421**: 38–53 (2019)

[16] Wang D G, Zhu H L, Xu W, Ye J H, Zhang D K, Abdel Wahab M. Contact and slip behaviors of main cable of the long-span suspension bridge. *Eng Fail Anal* **136**: 106232 (2022)

[17] Wang D G, Wang B, Gao W L, Ye J H, Abdel Wahab M. Dynamic contact behaviors of saddle materials for suspension bridge. *Eng Fail Anal* **134**: 106031 (2022)

[18] Liu Z X, Guo T, Han D G, Li A Q. Experimental study on corrosion-fretting fatigue behavior of bridge cable wires. *J Bridge Eng* **25**(12): 04020104 (2020)

[19] Guo T, Liu Z X, Correia J, de Jesus A M P. Experimental study on fretting-fatigue of bridge cable wires. *Int J Fatigue* **131**: 105321 (2020)

[20] Wang D G, Wang B, Xie G Z, Li C C, Zhang D K, Ge S R. Effect of temperature on tribo-corrosion behaviors of parallel steel wires of main cable in the suspension bridge. *Wear* **512–513**: 204522 (2023)

[21] Diomidis N, Celis J P, Ponthiaux P, Wenger F. Tribocorrosion of stainless steel in sulfuric acid: Identification of corrosion–wear components and effect of contact area. *Wear* **269**(1–2): 93–103 (2010)

[22] Jiang X X. Corrosion and wear of metal. In: *The Interaction of Metal Corrosion–wear*. Chen Z L, Ed. Beijing: Chemical Industry Press, 2003: 198–221.

[23] Hou X B, Wang Y X, Dai L Y, Yang Y H, Du J H, Wang Y J, Wan H. Study on the corrosion and wear behaviors of cylinder liner in marine diesel engine burning low sulfur fuel oil. *Eng Fail Anal* **147**: 107151 (2023)

[24] Feng C N, Zhang D K, Chen K, Guo Y B. Study on viscoelastic friction and wear between friction linings and wire rope. *Int J Mech Sci* **142–143**: 140–152 (2018)

[25] Feng C N, Zhang D K, Grecov D, Chen K. Effect of rheological properties of friction-enhancing greases on the friction between friction lining and wire rope. *Tribol Int* **144**: 106143 (2020)

[26] Zhao B, Zhang Y T, Fan Y Y, Yu X T, Zhang Z N, Zhang B C. The three-body abrasive tribological characteristics of the Graphene/h-BN heterostructure film considering defects. *Tribol Int* **171**: 107525 (2022)

[27] Shen, Y, Zhang, D K, Wang, D G, Xu, L M. Effect of contact load on the fretting wear behavior of steel wire. *Tribology* **30**(4): 404–408 (2010) (in Chinese)

[28] Li Z Y, Yu H Y, Sun D B. The tribocorrosion mechanism of aluminum alloy 7075-T6 in the deep ocean. *Corros Sci* **183**: 109306 (2021)

[29] Li Z Y, Yu H Y, Sun D B. Structural and microstructural effects produced by microwave sintering over La_2O_3 doped composites. *Ceram Int* **47**(19): 26692–26703 (2021)

[30] Wang W L, Cui W F, Xiao Z T, Qin G W. The improved corrosion and wear properties of Ti-Zr based alloys with oxide coating in simulated seawater environment. *Surf Coat Technol* **439**: 128415 (2022)

[31] Zhang Y Y, Descartes S, Chromik R R. Influence of WC on third body behaviour during fretting of cold-sprayed Cu MoS_2WC composites. *Tribol Int* **134**: 15–25 (2019)

[32] Jing P F, Yu S R, Zhang K F, Ma B H. Effects of load and displacement amplitude on fretting wear behavior of DLC film. *Tribology* **41**(2): 213–222 (2021) (in Chinese)

[33] Peng Y X, Chang X D, Sun S S, Zhu Z C, Mi Z T. The friction and wear properties of steel wire rope sliding against itself under impact load. *Wear* **400–401**: 194–206 (2018)

[34] Wang B, Wang D G, Chong H L, Xie G Z, Zhang D K, Ge S R. Tribo-corrosion interaction of the parallel steel wires in the suspension bridges. *Friction* **11**(12): 2221–2237 (2023)

[35] Wang B, Wang D G, Tang L, Chong H L, Xu W, Zhang X X, Zhang C L, Tan D L, Zhao X, Zhang D K, et al. Bending tribo-corrosion-fatigue behaviors between cable wire and saddle material in the suspension bridge. *Tribol Int* **187**: 108711 (2023)

[36] Guan J, Jiang X T, Xiang Q, Yang F, Liu J. Corrosion and tribocorrosion behavior of titanium surfaces designed by electromagnetic induction nitriding for biomedical applications. *Surf Coat Technol* **409**: 126844 (2021)

[37] Ferreira D F, Almeida S M A, Soares R B, Juliani L, Bracarense A Q, de Freitas Cunha Lins V, Junqueira R M R. Synergism between mechanical wear and corrosion on tribocorrosion of a titanium alloy in a Ringer solution. *J Mater Res Technol* **8**(2): 1593–1600 (2019)

[38] Chang X D, Peng Y X, Cheng D Q, Zhu Z C, Wang D G, Lu H, Tang W, Chen G A. Influence of different corrosive environments on friction and wear characteristics of lubricated wire ropes in a multi-layer winding system. *Eng Fail Anal* **131**: 105901 (2022)

Bo WANG. He received his M.S. degree in material processing engineering in 2019 from China University of Mining and Technology, Xuzhou, China. After then, he became a Ph.D. student in mechanical engineering in 2021 at the same university. His research interests include tribo-corrosion, corrosion-fatigue, and tribo-corrosion-fatigue of wire rope.

Dagang WANG. He received his M.S. and Ph.D. degrees in mechanical engineering from China University of Mining and Technology, Xuzhou, China, in 2009 and 2012, respectively. He joined China University of Mining and Technology from 2013. His current position is a professor and director of Mechanical Design Department. His research areas cover the surface-interface science and intelligent robot.